Nano Research

Open Access

Research Article

Starvation therapy-amplified photothermal therapy against colorectal cancer via GLUT1-mediated energy deprivation

Yanling Zhang[1], Yajie Sui[1], Shuang Wu[1], Qiong Huang[1], Mi Zou[1], Gege Zhang[1], Miaomiao Gao[1], Kecheng Zhou[1] ✉, Daoxiang Zhang[1] ✉, Xianwen Wang[2] ✉, and Pingping Liang[1] ✉

[1] *School of Life Sciences, Anhui Medical University, Hefei 230032, China*
[2] *School of Biomedical Engineering, Research and Engineering Center of Biomedical Materials, Anhui Medical University, Hefei 230032, China*

Cite this article: *Nano Research*, **2026**, *19*, 94908722. https://doi.org/10.26599/NR.2026.94908722

ABSTRACT: Photothermal therapy (PTT) has come into view as an innovative strategy for colorectal cancer (CRC) therapy based on its exceptional spatial selectivity and minimal side effects. However, clinical PTT is severely restricted due to the limited depth of laser penetration and the self-protective nature of cells with heat shock protein (HSP) upregulation. Herein, we prepared a synergistic PTT/ST near-infrared (NIR) nanoplatform (PR NPs), which is self-assembled from the NIR phototherapeutic agent PPAB and the glucose transporter 1 (GLUT1) inhibitor resveratrol (RES) to fight CRC. The PR NPs display enhanced cancer PTT efficiency owing to the downregulation of adenosine triphosphate (ATP)-dependent HSPs mediated by RES. Meanwhile, the enhanced metabolism and energy consumption triggered by PTT further exacerbate the energy crisis, amplifying the starvation therapy (ST) effect. More significantly, the RES released from PR NPs can also specifically target GLUT1 in CRC cells to promote apoptosis and suppress migration. Hence, the versatile NIR PR NPs can simultaneously enable efficient photothermal ablation and precise energy deprivation to improve antitumor outcome, providing a novel paradigm for CRC treatment.

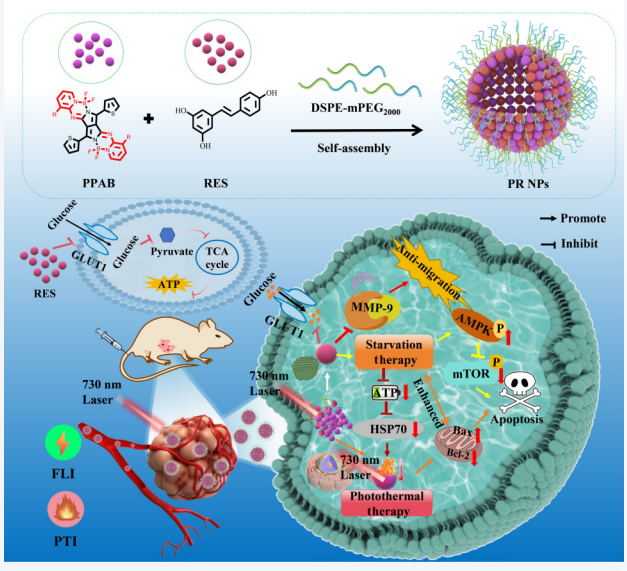

KEYWORDS: glucose transporter 1, energy deprivation, starvation therapy, photothermal therapy, colorectal cancer

1 Introduction

Colorectal cancer (CRC), the third most common malignant tumor globally, places a heavy burden on global health owing to its high incidence and mortality rates, with an unfavorable prognosis and an approximate 5-year survival rate of 65% [1, 2]. At present, CRC treatment primarily relies on surgery supplemented by chemoradiotherapy, targeted therapy, and immunotherapy, but therapeutic outcomes remain suboptimal due to tumor heterogeneity and drug resistance, with ~ 30%–50% of patients experiencing local recurrence or distant metastasis, which poses great challenges to clinical management [3–6]. Although precise photothermal therapy (PTT) is an advanced non-invasive modality for CRC treatment via hyperthermia generated by phototherapeutic agents (PTAs) under near-infrared (NIR) laser irradiation with minimum side effects [7–11], it is restricted by the limited depth of laser penetration and increased expression of heat shock proteins (HSPs) [12–15]. In recent years, nanotechnology-based PTAs with unique physicochemical properties, such as controllable particle size distribution and adjustable composition [16–19], have achieved stable blood circulation, selective passive targeting, and highly efficient drug accumulation *in vivo* to improve metabolic behaviors and reduce side effects via the enhanced permeability and retention

Received: February 14, 2026; **Revised:** April 3, 2026
Accepted: April 8, 2026

✉Address correspondence to Kecheng Zhou, zhoukecheng@ahmu.edu.cn; Daoxiang Zhang, hooray365@163.com; Xianwen Wang, xianwenwang@ahmu.edu.cn; Pingping Liang, liangpingping@ahmu.edu.cn

(EPR) effect [20–22], which can initiate more precise CRC photo-ablation.

Additionally, the rapid proliferation of malignant tumor cells is closely dependent on energy metabolism, implying that starvation therapy (ST), which can deplete glucose and inhibit energy generation, is an innovative non-invasive method to fight cancer [23–25]. However, the traditional glucose oxidase (GOx)-based ST is severely restrained by the limited catalytic activity of GOx at physiological temperature and in the hypoxic tumor microenvironment (TME) [26, 27]. Significantly, glucose transporter 1 (GLUT1) is a key protein that regulates cellular glucose uptake, which exhibits high expression in diverse solid tumors and is considered an excellent target for tumor ST [28–30]. Herein, the inhibition of GLUT1-mediated glucose transport can reduce the energy supply to weaken tumoral mitochondrial function and continuously promote cancer ST [31]. Moreover, under thermal stress, tumor cells accelerate metabolism and energy consumption for hyperthermia tolerance, which can further amplify the ST effect [32]. Meanwhile, the reduction in glucose supply will prevent the generation of adenosine triphosphate (ATP) and downregulate the expression of ATP-dependent HSPs in tumor cells, which can effectively boost the PTT effect [33].

Notably, resveratrol (RES) is one of the most extensively studied natural compounds as a GLUT1 inhibitor, and is a polyphenolic plant-derived compound with significant biological activity to inhibit cell proliferation [34, 35]. Besides, RES can trigger a hypoxic TME with limited glucose uptake and lactate production to initiate cellular autophagy [36, 37]. Additionally, it can also interfere with mitochondrial respiration to impede ATP production thereby restricting migration and invasion, and promoting cellular apoptosis [38]. However, due to the presence of multiple phenolic hydroxyl groups in the RES structure, it exhibits drawbacks such as low bioavailability, poor stability, and undesired tumor specificity when administered alone [39]. Therefore, it is significant to conjugate RES with other excellent therapeutic drugs for synergistic cancer treatment. Diketopyrrolopyrrole (DPP), as a donor–acceptor–donor (D–A–D) type zwitterionic compound, has a series of planar π-conjugated derivatives, exhibiting strong NIR absorption with a low energy gap, desired photothermal performance, superb stability, and excellent fluorescence imaging (FLI) property, showing broad application prospects in bioimaging-guided cancer phototherapy [40].

Hence, we prepared the multifunctional NIR nanoparticles (PR NPs) for the ST-amplified PTT to fight CRC. Herein, the conjugated PPAB exhibits dual photothermal imaging/fluorescence imaging (PTI/FLI) property with excellent photothermal effect, which can self-assemble with the GLUT1 inhibitor RES into PR NPs for enhanced CRC photo-ablation with mitochondrial dysfunction to suppress energy production, enhancing the ST effect. Notably, RES released after irradiation can target GLUT1 to reduce cellular glucose uptake, boost the starvation effect, regulate P-AMPK/P-mTOR levels, improve Bax expression, and prevent Bcl-2 signaling for effective cellular apoptosis, as well as decrease matrix metalloproteinase-9 (MMP-9) expression to suppress cellular migration. More significantly, the diminished ATP generation will downregulate HSP expression to augment CRC PTT. Moreover, PR NPs display superb phototoxicity, low dark toxicity, and favorable biocompatibility *in vitro*, consequently enabling efficient tumor ablation guided by multimodal PTI/FLI *in vivo* (Scheme 1).

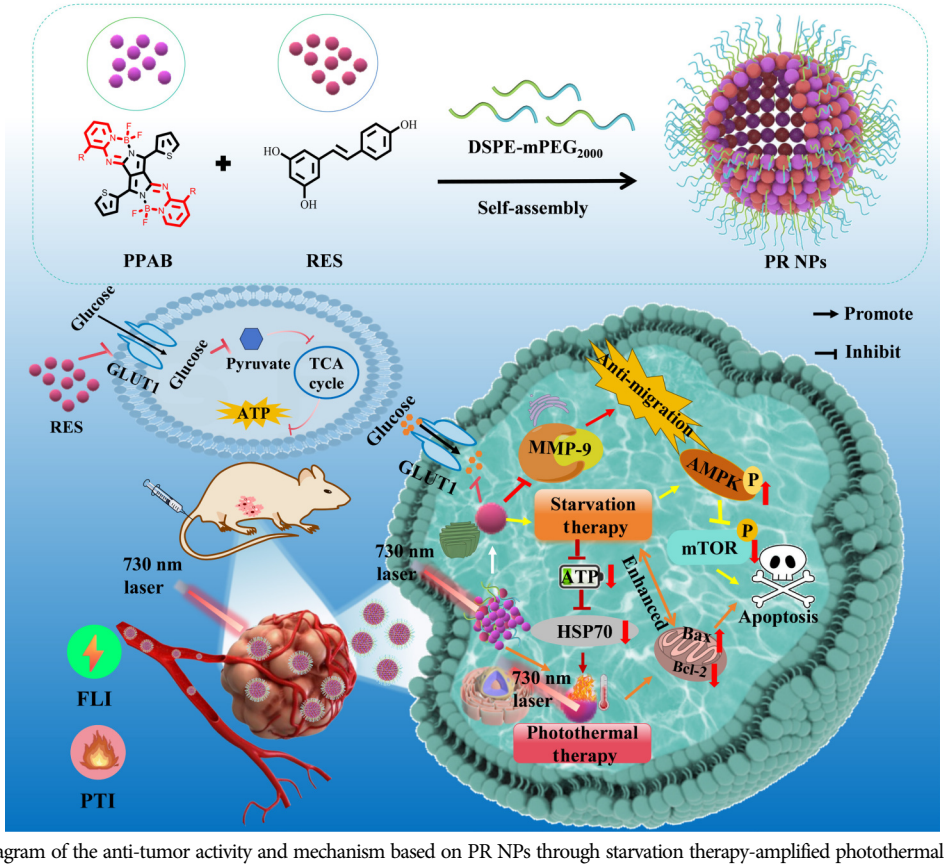

Scheme 1 Schematic diagram of the anti-tumor activity and mechanism based on PR NPs through starvation therapy-amplified photothermal therapy against CRC by GLUT1-mediated energy deprivation.

2 Results and discussion

2.1 Synthesis, spectral, structural, and photothermal properties

We synthesized the NIR photosensitizer PPAB molecule based on the DPP structure (Fig. S1 in the Electronic Supplementary Material (ESM)) [41]. Initially, 2-amino-3-hydroxypyridine was reacted with 7-(bromomethyl)-pentadecyl to obtain 3,3'-diaminobenzidine (DAB), and followed by reaction with DPP-1 to acquire PPAB with a yield of 54%. Then the DAB and PPAB molecule structures were confirmed through the ^{1}H nuclear magnetic resonance (NMR) and matrix-assisted laser desorption/Ionization time-of-flight (MALDI-TOF) mass spectrometry, wherein the hydrogen atom counts, chemical shifts, and relative molecular masses matched theoretical values, demonstrating the structural accuracy and high purity of the synthesized compounds (Figs. S2–S4 in the ESM). In addition, spectroscopic detection reveals that free PPAB molecule exhibits a wide NIR absorption band (λ_{max}: 692 nm) with a molar extinction coefficient of 7.7286×10^4 $M^{-1}\cdot cm^{-1}$ based on the Beer–Lambert law, presenting excellent light-absorbing capacity (Figs. S5(a) and S5(b) in the ESM). Furthermore, PPAB molecule and PR NPs display bright fluorescent emission with λ_{max} at 725 nm, indicating bioimaging ability (Fig. S5(c) in the ESM). The self-assembled PR NPs were prepared by the reprecipitation technology based on free PPAB and RES with 1,2-distearoyl-*sn*-glycero-3-phosphoethanolamine-poly(ethylene glycol) (DSPE-mPEG$_{2000}$) (Fig. 1(a)). Herein, the absorbance spectrum of PR NPs contains NIR absorption bands ranging from 500 to 800 nm with λ_{max} at 727 nm affiliated PPAB NPs, as well as 312 nm absorbance from RES NPs, showing the J-aggregation between free PPAB molecules and strong conjugated planarization as well as π–π stacking interaction between PPAB and RES molecules within the nanoparticles (Fig. 1(b)), which contributes to enhanced stability and photothermal conversion efficiency of PR NPs. Moreover, PR NPs were found to have a molar extinction coefficient of 6.4152×10^4 $M^{-1}\cdot cm^{-1}$, indicating a strong laser absorption property for superb NIR photothermal conversion (Figs. 1(f) and 1(g)). Transmission electron microscopy (TEM) characterization of PR NPs exhibits uniform spherical morphology with excellent dispersibility (Fig. 1(c)). Dynamic light scattering (DLS) measurement reveals that PR NPs display a mean particle diameter of 111.6 nm (PDI: 0.305) with a narrow size distribution and zeta potential of −26.67 mV (Figs. 1(d) and 1(e)), which can promote internalization at the tumor site by the passive targeting effect with long-term blood circulation for desired tumor suppression. Besides, the color, average size, and absorbance of PR NPs could stably maintain no obvious change within 7 days at 4 °C, further demonstrating the good morphological stability (Figs. 1(h) and 1(i)).

Theoretical calculation of the energy gap demonstrates that the D–A–D PPAB organic molecule can effectively reduce the electron density overlap between the highest occupied molecular orbital (HOMO) and lowest unoccupied molecular orbital (LUMO) with ΔE of 1.99 eV, which indicates it will stimulate ideal non-radiative thermal release transitions (Fig. 1(j)). Subsequently, we conducted the photothermal properties of PR NPs in Figs. 1(k)–1(l), which display the temperature change processes of PR NPs (+) with increasing concentrations (5, 10, 15, 30, and 60 μM), and the temperature increases are 18.2, 27.1, 28.1, 30.2, and 31.1 °C, respectively. Moreover, the temperature of PR NPs (60 μM) increased by 5.7, 12.9, 18.8, 24.9, and 31.1 °C under laser irradiation at 0.2, 0.4, 0.6, 0.8, and 1.0 W/cm^2, respectively. The above results prove a superb photothermal effect with obvious concentration and power-density dependence. Afterwards, the η (photothermal conversion efficiency) of PR NPs was calculated as 65.7% (Fig. 1(m) and Fig. S5(d) in the ESM), which is significantly higher than that of PPAB NPs (60.99%, Figs. S6(c) and S6(d) in the ESM) and some reported PTAs [42]. Additionally, it shows no significant changes in the temperature rises, color, or ultraviolet (UV) spectrum of the PR NPs dispersion after five cycles of alternate irradiation (laser on: 5 min, and off: 5 min), confirming excellent photothermal stability (Fig. 1(n) and Fig. S5(e) in the ESM). Furthermore, the PTI capability of PR NPs enhances with increasing concentration, indicating that this nanodrug holds potential for PTI-guided *in vivo* tumor therapy (Fig. 1(o)).

2.2 The expression of GLUT1 and survival prognosis in CRC

To explore GLUT1 expression and its correlation with prognosis in CRC, 31 cancer tissues and their corresponding normal counterparts were initially compared based on Gene Expression Profiling Interactive Analysis (GEPIA) data, which displays significant differences (Fig. 2(a)). Furthermore, the Human Protein Atlas (HPA) database analyzed approximately 29 types of tumor tissues, revealing that the expression level of GLUT1 exhibits tumor specificity and is highly expressed in the SW480 CRC subtype (Figs. 2(b) and 2(c)). In addition, survival association analysis based on the GEPIA database was performed to investigate how GLUT1 expression correlates with patient prognosis. As shown in Fig. 2(d), elevated GLUT1 expression was notably associated with shorter overall survival and poorer prognostic outcomes in CRC patients. Notably, immunohistochemical data from the HPA database demonstrate significantly higher GLUT1 protein expression in CRC tissue compared with that in normal colon tissue (Fig. 2(e)). Furthermore, Western blot analysis of five cell lines (CRC cells: SW480 and HCT116; gastric cancer cells: MKN45; normal cells: HUVEC and GES-1) confirms higher GLUT1 expression in SW480 cells, providing strong evidence for its potential as a therapeutic target in CRC (Figs. S7(a) and S7(b) in the ESM).

2.3 *In vitro* cytotoxicity, cellular uptake, and anti-cancer performance of PR NPs

Inspired by the superb physicochemical properties of PR NPs, the cytotoxicity and anti-cancer performance *in vitro* were evaluated (Fig. 3(a)). Firstly, the cytotoxicity of PR NPs toward SW480 cells was evaluated by the 3-(4,5-dimethylthiazol-2-yl)-2,5-diphenyltetrazolium bromide (MTT) assay. As demonstrated in Fig. 3(b), compared to the IC_{50} (half-maximal inhibitory concentration) of 20.89 μM triggered by PPAB NPs (+), the cell viability significantly decreases with dosage dependence and induces an IC_{50} of 4.285 μM incubated by PR NPs (+), presenting synergistic cellular ablation effect. Besides, the cell viability still remains at ~ 100% even at high drug concentration (8 μM), demonstrating excellent biocompatibility and low dark toxicity of PPAB NPs (−). In contrast, the cell viabilities exhibit slightly concentration-dependent decreases in RES NPs and PR NPs (−) groups, which is attributed to RES-mediated glucose uptake inhibition and consequent energy depletion, triggering cellular

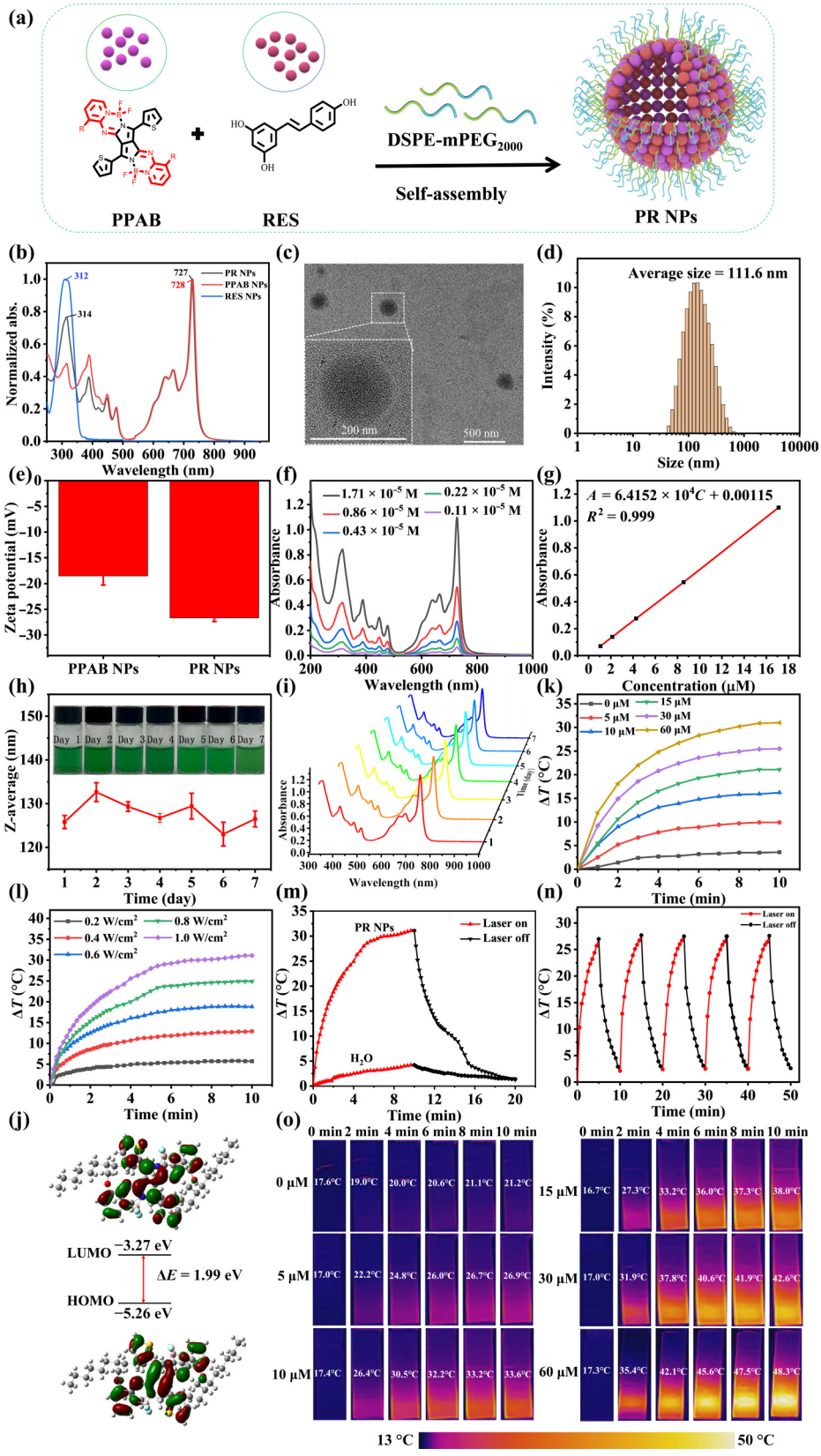

Figure 1 Synthesis, spectral, structural, and photothermal properties of PR NPs. (a) Preparation schematic of PR NPs. (b) Absorbance curves of RES NPs, PPAB NPs, and PR NPs in ddH_2O. (c) TEM image, (d) hydrated particle size, and (e) zeta potential of PR NPs. (f) Absorbance curves of PR NPs at different concentrations and (g) the linear absorbance versus concentration. (h) Photographs, hydrated particle size, and (i) characteristic UV absorption peak changes of PR NPs within 7 days (n = 3). (j) Calculated HOMO–LUMO energy gap of PPAB. Photothermal changes of PR NPs at (k) different concentrations and (l) different laser power densities. (m) The heating and cooling curves of PR NPs (+) and ddH_2O during laser on and off (1 mL, 60 μM, 1.0 W/cm^2). (n) Photothermal temperature changes of PR NPs (+) (60 μM) after five laser switching cycles. (o) Infrared thermal imaging of PR NPs (+) solution (1 mL) at different concentrations.

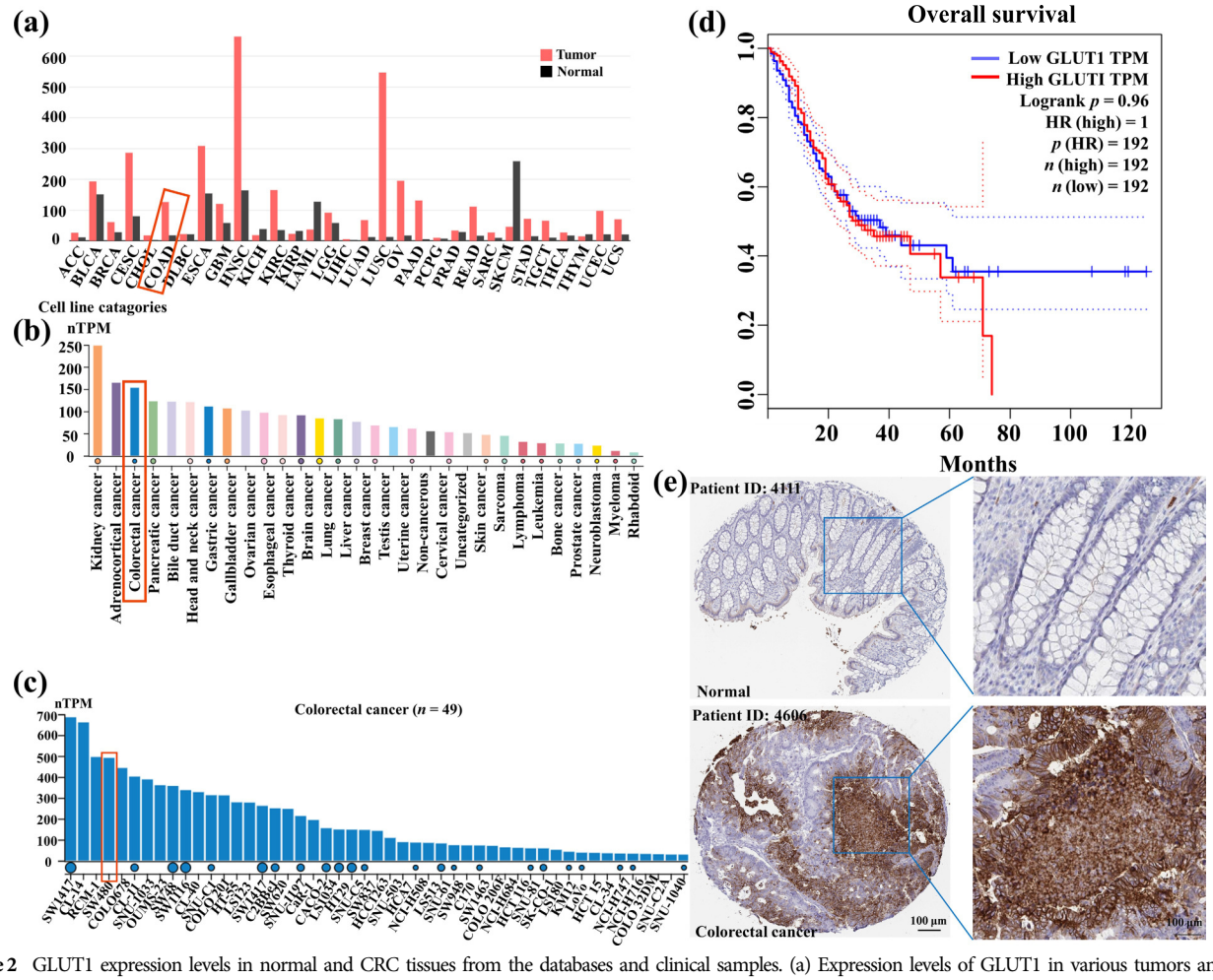

Figure 2 GLUT1 expression levels in normal and CRC tissues from the databases and clinical samples. (a) Expression levels of GLUT1 in various tumors and their adjacent normal tissues from the GEPIA database. (b) GLUT1 gene expression levels in 29 different tumor types based on the HPA database. (c) GLUT1 gene expression levels of 49 different CRC subtypes based on the HPA database. (d) Correlation of GLUT1 gene expression with overall survival in CRC patients from the GEPIA database. (e) GLUT1 protein levels in colon and CRC samples from the HPA database (scale bars: 100 μm).

proliferation suppression (Fig. 3(c)). Moreover, we further assessed the dark toxicity of PR NPs on normal cells (HUVEC, 293T, GES-1, and L929), which shows no obvious viability reduction with dosage increasing, owing to the inherently low GLUT1 expression in normal cells and the non-acidic TME that limits RES activity, confirming the favorable biosafety of PR NPs (Fig. 3(d)). Besides, a hemolysis assay was initially employed to assess the *in vivo* biosafety of PR NPs, which reveals that the hemolysis rates of red blood cells are all significantly lower than those of the positive control (ddH_2O) and 5% (permissible limit) when the concentration of PR NPs increased from 5 to 120 μM, further verifying the superb biocompatibility of the therapeutic NPs (Fig. 3(e)) [43]. Furthermore, to detect live/dead (green/red) cells after PR NPs treatment, the SW480 cells were irradiated and incubated with calcein-acetoxymethyl ester/propidium iodide (Calcein-AM/PI). As illustrated in Figs. 3(f) and 3(g), more apoptotic cells in the PR NPs (+) groups (2, 4, and 8 μM) are observed with concentration dependence compared with the control group (0 μM), highlighting the excellent synergistic cell ablation capacity of PR NPs. Additionally, annexin V-fluorescein isothiocyanate/propidium iodide (Annexin V-FITC/PI) staining was performed to further quantitatively investigate cellular apoptosis induced by PR NPs. Figs. 3(h) and 3(i) show that the cell apoptosis rate displays a dose-dependent increase, with significant percentages of 8.3%, 16.8%, 35.9%, and 89.4%, respectively; meanwhile, the quantitative fluorescence values of PI in different groups are presented in Fig. 3(j), which demonstrates that PR NPs can effectively induce cell apoptosis.

Motivated by the bright fluorescence signal of PR NPs, confocal laser scanning microscopy (CLSM) and flow cytometry were employed to monitor the cellular internalization of the nano-agent. Figure 3(k) exhibits that the PR NPs group exhibits brighter cytoplasmic fluorescence than the control group, indicating effective uptake of PR NPs by SW480 cells, which is crucial for biological imaging and is expected to guide *in vivo* FLI. Consistently, the quantitative fluorescence result from flow cytometry also demonstrates that PR NPs can rapidly accumulate in the cellular cytoplasm, further indicating the bio-imaging effect (Figs. 3(l) and 3(m)).

2.4 ST of PR NPs *in vitro*

To investigate the starvation effect associated with the inhibition of GLUT1-mediated glucose transport triggered by PR NPs during the therapy (Fig. 4(a)), Figs. 4(b) and 4(c) show that the intracellular glucose and ATP levels significantly decrease with increasing PR NPs concentration in SW480 cells, indicating the effective

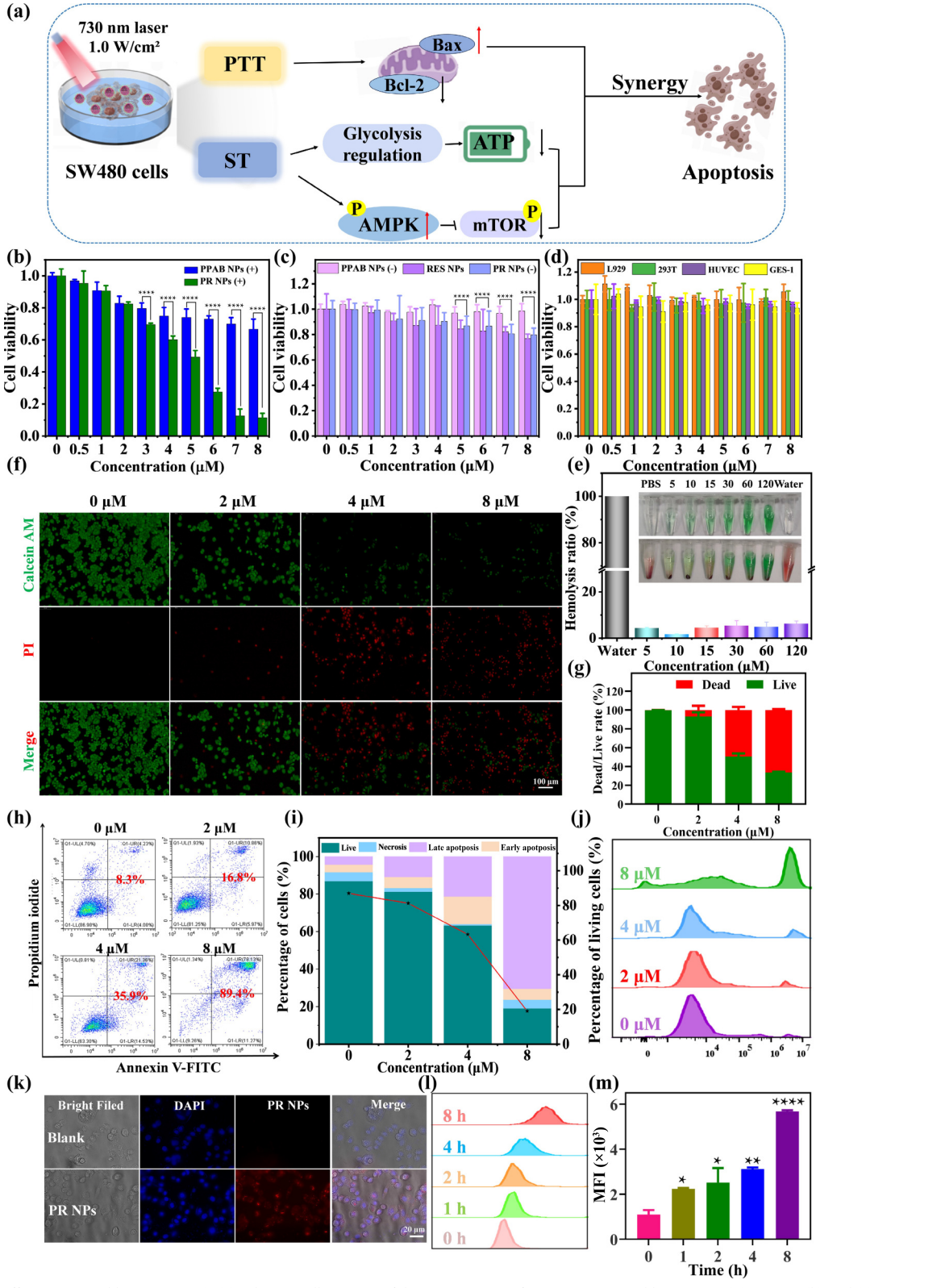

Figure 3 Cytotoxic effects motivated by PR NPs (+). (a) Schematic illustration of the anti-tumor performance motivated by PR NPs (+) *in vitro*. (b) and (c) MTT assay of SW480 CRC cells (730 nm laser, 1.0 W/cm²) under different conditions. (d) MTT assay of different cells treated with PR NPs (−). (e) Hemolysis assay of fresh mouse RBCs co-incubated with PR NPs at different concentrations. The bottom panel shows RBC suspensions after co-incubation with PR NPs and centrifugation, whereas the top panel shows PR NPs alone at the corresponding concentrations after centrifugation. (f) Fluorescence imaging and (g) quantification of SW480 cells co-stained with Calcein-AM and PI induced by various concentrations of PR NPs (+) (scale bar: 100 μm). (h) Flow cytometry analysis and (i) quantification of SW480 cells co-incubated with PR NPs (+). (j) Quantitative analysis of PI fluorescence at diverse concentrations. (k) CLSM images of SW480 cells treated with PR NPs (8 μM) for 4 h (scale bar: 20 μm). (l) Quantitative flow cytometry analysis and (m) mean fluorescence intensity (MFI) of PR NPs in SW480 CRC cells at different time points. Data are shown as mean ± standard deviation (SD). The *P* values were determined using two-way ANOVA. **P* < 0.05, ***P* < 0.01, ****P* < 0.001, *****P* < 0.0001.

inhibition of glucose transport triggered by RES and the consequent reduction in ATP synthesis under starvation conditions. Since the migration of cancer cells is closely related to energy production, the wound healing assay and Transwell assay were further employed *in vitro*. As shown in Figs. 4(d) and 4(e), cell migration at the same time point gradually decreases in a drug concentration-dependent manner, wherein the scratch healing rate of the 8 μM group after 48 h is only 13.76%, which is significantly lower than that of the control group (52.17%). Furthermore, the result of the Transwell assay displays that the number of cells migrating from the upper chamber to the lower chamber also progressively decreases as PR NPs concentration increases (Figs. 4(f) and 4(g)). All the above results indicate that PR NPs can effectively inhibit the migration of SW480 cells, further proving the effective suppression of energy production induced by PR NPs in tumor cells.

2.5 Mitochondrial dysfunction and metabolomics

It is known that MMP (mitochondrial membrane potential) acts as a characteristic indicator of mitochondrial function. In cases of high MMP, 5,5',6,6'-tetrachloro-1,1',3,3'-tetraethylbenzimidazolyl-carbocyanine iodide (JC-1) aggregates in the mitochondrial matrix of healthy cells and emits red fluorescence. Conversely, JC-1 exists as monomers in the cytoplasm with green fluorescence in dysfunctional cells (Fig. 5(a)) [44]. As presented in Fig. 5(b), the red/green fluorescence ratio in SW480 cells gradually declines in the groups of control, PPAB NPs (+), and PR NPs (+), indicating severe mitochondrial dysfunction mediated by the synergistic effect of PR NPs. Meanwhile, biological transmission electron microscopy (Bio-TEM) monitoring for the morphological changes of mitochondria shows that the mitochondria in the control group have intact structures with uniform cristae distribution [45]. However, blurred cristae, visible vacuolization, and significant degeneration with decreased mitochondrial length as well as increased damage are observed in the PR NPs (+) group, clearly indicating mitochondrial dysfunction (Figs. 5(c)–5(e)).

To investigate the mechanism of metabolism alterations in mitochondrial energy metabolism mediated by PR NPs *in vitro*, we performed a comprehensive metabolomic analysis (Fig. 6(a)) [46]. Principal component analysis (PCA) was initially conducted to assess the quality and variability of metabolic profiles, which demonstrates significant sample segregation into two distinct clusters (control and PR NPs (+)), suggesting significant alterations in the cellular metabolome after treatment (Fig. 6(b)). Hence, volcano plots show that 473 differentially expressed metabolites were detected after PR NPs (+) treatment, wherein 292 of them are upregulated metabolites (red dots), and 181 are downregulated metabolites (blue dots), indicating meaningful metabolic reprogramming during the synergistic cancer therapy (Fig. 6(c)). Besides, variable importance in projection (VIP) analysis identifies significantly different metabolites, mainly involving amino acids, lipid metabolism, and energy-related substances, which are related to key biological processes such as energy metabolism, lipid remodeling, and amino acid turnover (Fig. 6(d)). In addition, the differential metabolite heatmap displays that the expression of apoptosis-related cytidine monophosphate (an intermediate product of pyrimidine nucleotide metabolism) and energy-related phosphocholine (a precursor for phosphatidylcholine synthesis that affects mitochondrial function) is upregulated, showing cellular apoptosis and decreased ATP production with mitochondrial dysfunction initiated by PR NPs (+) (Fig. 6(e)). Furthermore, Kyoto Encyclopedia of Genes and Genomes (KEGG) pathway enrichment analysis was employed to identify the most significantly enriched pathways among the differentially expressed metabolites. Figure 6(f) reveals that the differentially expressed metabolites after PR NPs (+)

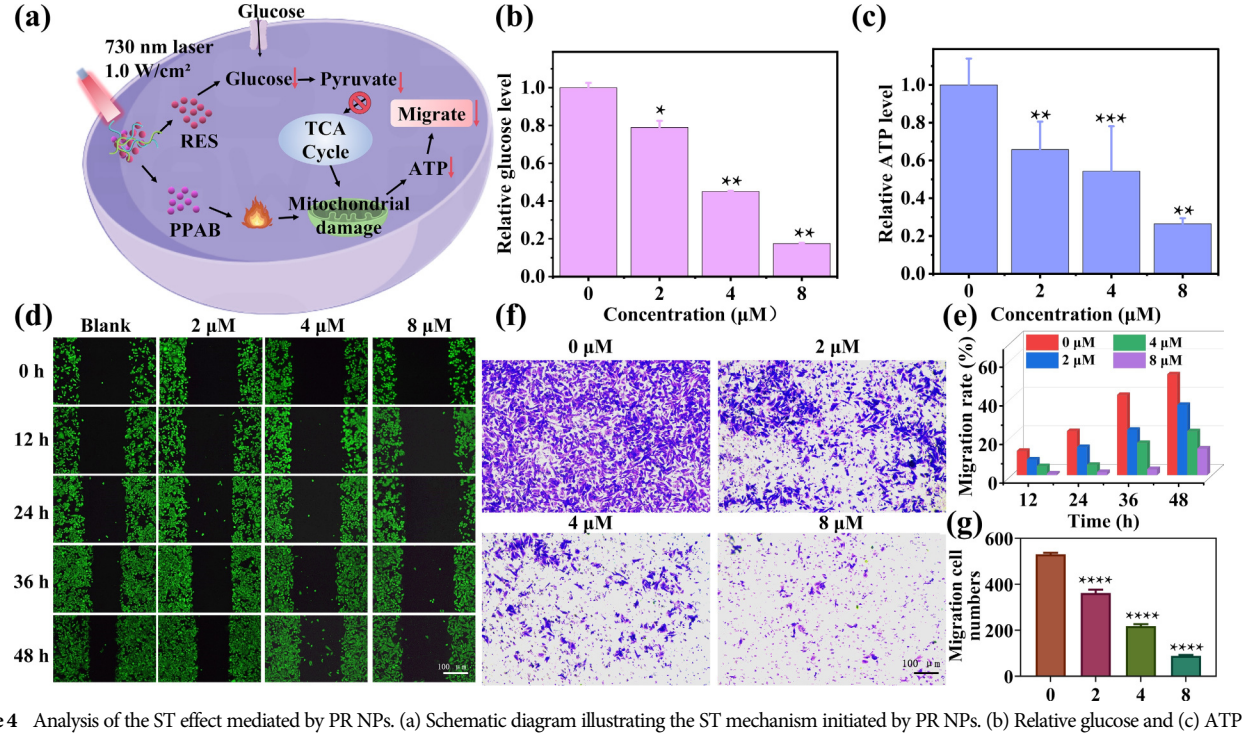

Figure 4 Analysis of the ST effect mediated by PR NPs. (a) Schematic diagram illustrating the ST mechanism initiated by PR NPs. (b) Relative glucose and (c) ATP levels in SW480 cells exposed to different PR NPs concentrations. (d) Images and (e) migration rates of the wound healing process in SW480 cells at various PR NPs concentrations (scale bar: 100 μm). (f) Transwell assay and (g) quantification of migration activity in SW480 cells exposed to varying PR NPs concentrations (scale bar: 100 μm). Data are shown as mean ± SD. The *P* values were determined using two-way ANOVA. **P* < 0.05, ***P* < 0.01, ****P* < *0.001*, *****P* < 0.0001.

treatment are enriched in the pathways of "alanine, aspartate and glutamate metabolism" to supply intermediates for the tricarboxylic acid cycle, thermogenesis, and oxidative phosphorylation, indicating the reprogramming of energy metabolism. Moreover, pathway enrichment of "Choline metabolism in cancer" and "ABC transporters" implies that PR NPs (+) regulate cellular apoptosis through choline metabolism and imbalance of metabolite transport. Overall, the systematic differential metabolite analysis displays obvious metabolic reprogramming to regulate energy generation mainly through amino acid and phospholipid metabolism, as well as cellular apoptosis mainly through altering nucleotide and lipid metabolism, which will boost the mechanistic study of tumor therapy mediated by PR NPs.

2.6 *In vitro* anti-tumor molecular mechanism of PR NPs

To further confirm that the signal transduction pathways triggered by RES from PR NPs are critical to cancer progression and regulate cell apoptosis, proliferation, and migration, the Western blot (WB) assay was employed to assess the expression level of energy-related proteins: glucose transport-related protein (GLUT1), heat shock protein 70 (HSP70), apoptosis-related proteins: Bax, Bcl-2, phosphorylated adenosine monophosphate-activated protein kinase (P-AMPK), phosphorylated mammalian target of rapamycin (P-mTOR), and the migration-related protein: MMP-9 (Fig. 7(a)). Figures 7(b)–7(l) demonstrate that GLUT1 and HSP70 expression levels are significantly reduced in a PR NPs concentration-dependent manner relative to the control group, indicating reduced glucose transport and insufficient mitochondrial energy supply

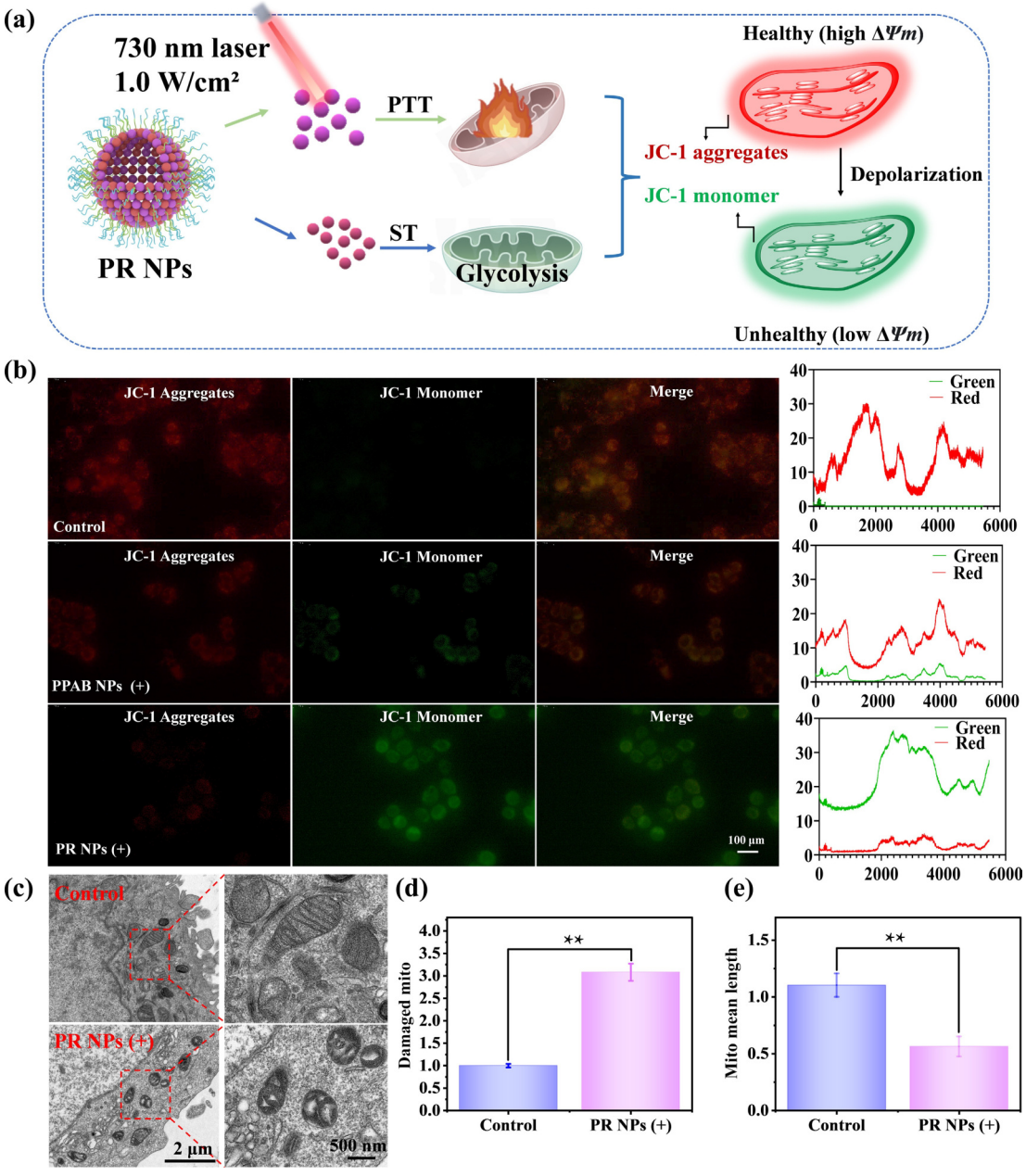

Figure 5 Mitochondrial dysfunction. (a) Schematic illustration of the mitochondrial dysfunction induced by PR NPs (+). (b) MMP evaluation by JC-1 staining in SW480 cells following various treatments (scale bar: 100 μm). (c) Bio-TEM images of mitochondrial morphology in SW480 cells treated with PBS (control) or PR NPs (+). Quantification of (d) damaged mitochondria and (e) mitochondrial mean length based on panel (c).

leading to decreased ATP production, which further downregulates HSP70 generation in tumor cells for promoted PTT effect. Furthermore, the expression of pro-apoptotic proteins (P-AMPK and Bax) is upregulated, while that of anti-apoptotic proteins (Bcl-2 and P-mTOR) is downregulated, suggesting significant cellular apoptosis induced by PR NPs. In addition, the expression of MMP-9 (dependent on energy metabolism) is also decreased, which can inhibit cell migration, implying suppressed tumor metastasis induced by PR NPs *in vivo*.

2.7 *In vivo* biodistribution and therapeutic efficacy of PR NPs

Motivated by the superb properties of PR NPs *in vitro*, the SW480 tumor-bearing nude mouse model was further constructed to comprehensively evaluate the *in vivo* biodistribution and anti-tumor efficacy of PR NPs. Initially, based on the strong NIR fluorescence signal of PR NPs *in vitro*, FLI of PR NPs at different concentrations was analyzed to assess biodistribution. Figure S5(f) in the ESM demonstrates that the fluorescence intensity of the NIR nanomedicine exhibits a concentration-dependent enhancement, holding potential for FLI-guided *in vivo* tumor therapy. Afterwards, the NIR fluorescence signal of PR NPs at the tumor site gradually increases and reaches a maximum at 3 h due to the EPR passive targeting, offering an optimal treatment window to guide tumor therapy *in vivo*, wherein the liver fluorescence is attributed to its role as an important metabolic organ, proving the desired biocompatibility and metabolic capability of PR NPs *in vivo* (Figs. 8(b)–8(e)). To further verify the EPR-targeting capability of PR NPs, PTI at the tumor site was executed by a 730 nm laser (1.0 W/cm^2) at 3 h post-intravenous injection. As depicted in Figs. 8(f) and 8(g), the tumor temperature rises steadily to 54.3 °C within 6 min (ΔT = 18.3 °C), while only a slight temperature increase is observed in the control group (ΔT = 4.8 °C), which fully demonstrates that PR NPs possess high photothermal conversion efficiency with excellent PTI property based on the EPR effect, implying effective cancer PTT *in vivo*.

Hence, the SW480 tumor-bearing mice were randomly assigned to 5 groups (n = 5): (I) PBS as the control group, (II) RES NPs, (III) PR NPs (–), (IV) PPAB NPs (+), (V) PR NPs (+), and the

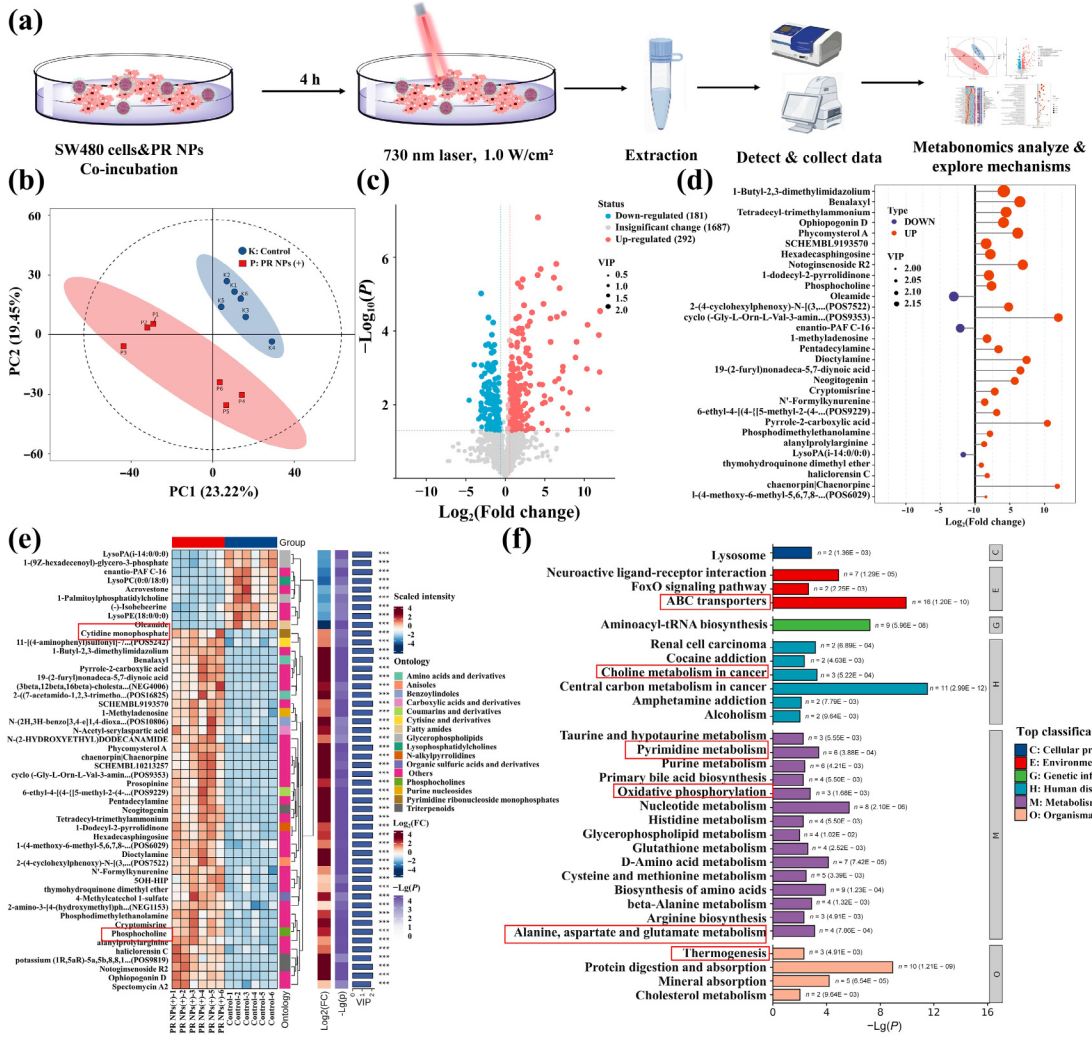

Figure 6 Exploration of the therapeutic mechanisms of PR NPs through metabolomic analysis. (a) Schematic diagram of the metabolomics analysis workflow. (b) PCA of the control group (blue) and the PR NPs (+) group (red), indicating distinct metabolic profiles. (c) Volcano plot of differentially expressed metabolites in SW480 cells treated with PR NPs (+) compared to the control group. Red dots denote upregulated metabolites, whereas blue dots represent downregulated ones. (d) Fold change and VIP scores for the top 30 metabolites. (e) The heatmap illustrates the heterogeneity in metabolite levels across different groups (n = 6). (f) KEGG pathway enrichment analysis in the different groups.

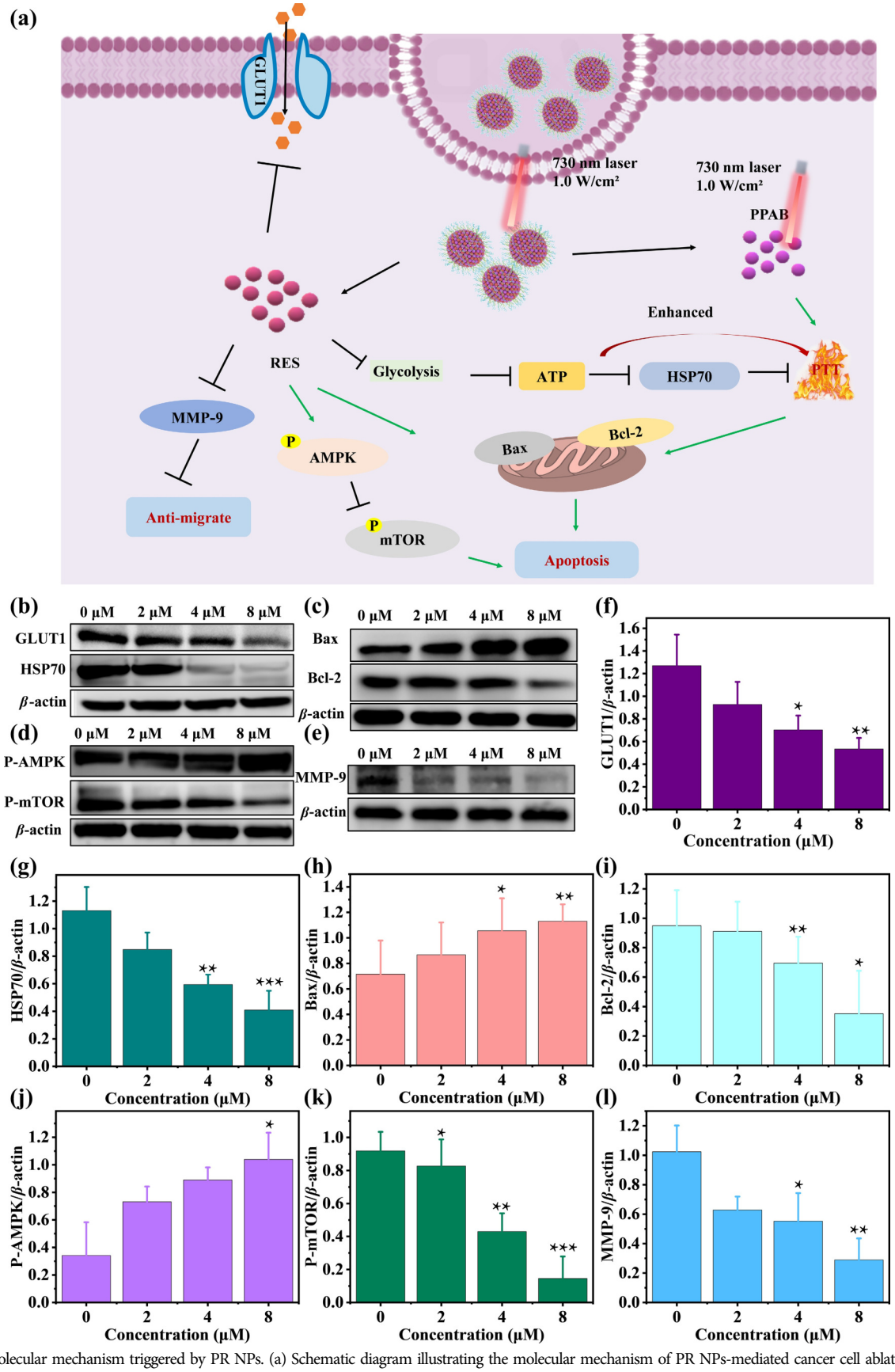

Figure 7 Molecular mechanism triggered by PR NPs. (a) Schematic diagram illustrating the molecular mechanism of PR NPs-mediated cancer cell ablation. Western blot analysis of (b) GLUT1, HSP70, (c) Bax, Bcl-2, (d) P-AMPK, P-mTOR, and (e) MMP-9 expression in SW480 cells treated with PR NPs (+) at different concentrations ($n = 3$), with β-actin as the loading control. (f)–(l) Relative quantification of gray values of protein band intensities. Data are shown as mean ± SD ($n = 3$). $^{*}P < 0.05$, $^{**}P < 0.01$, $^{***}P < 0.001$.

treatment procedure over 16 days is illustrated in Fig. 8(a). As presented in Figs. 8(h)–8(k), the RES NPs and PR NPs (–) groups exhibit a slight tumor inhibition compared with the control group, but the tumors in the PPAB NPs (+) and PR NPs (+) groups are significantly suppressed, and more notably, all tumors are completely eliminated in the PR NPs (+) group after the second treatment with no recurrence, revealing an amplified tumor ablation effect of PR NPs *in vivo*. Besides, there are no significant differences in body weights of all the mice over the treatment period, indicating negligible systemic toxicity (Fig. 8(l)). Additionally, no obvious differences in hematological, liver function, and kidney function parameters between the control and PR NPs (+) groups were detected, further confirming no infection, inflammation, or systemic side effects during treatment (Fig. 8(m)). Meaningfully, hematoxylin and eosin (H&E) staining of major organs (heart, liver, spleen, lung, and kidney) further verifies no systemic toxicity of these therapeutic agents (Fig. S8 in the ESM). Moreover, tumor tissues from various groups were evaluated by H&E staining, terminal deoxynucleotidyl transferase dUTP nick end labeling (TUNEL) assay, and Ki-67 immunohistochemistry, which show more apoptotic cells with prominent vacuolization and intercellular spaces in the PR NPs (+) group than in other groups, further proving the augmented anti-tumor efficiency of PR NPs (Fig. 8(n)). Finally, the expression levels of GLUT1 and HSP70 are significantly downregulated in the RES NPs, PR NPs (–), and PR NPs (+) groups, which indicates that RES can significantly downregulate GLUT1 expression to reduce the ATP production for HSP70 inhibition, ultimately decreasing the photothermal tolerance of tumor cells to improve the photothermal ablation effect (Fig. 8(o)). All the above experiments consistently demonstrate that PTT enhanced by PR NPs-mediated ST exhibits high tumor ablation efficacy and holds great potential for clinical application in CRC therapy.

3 Conclusions

In summary, we have successfully established PR NPs, which are assembled by the GLUT1 inhibitor RES and the phototherapeutic agent PPAB to initiate NIR laser-activated cancer ST combined with PTT. Herein, the RES released from the PR NPs can inhibit GLUT1 expression to suppress glucose uptake for tumor inhibition *via* ST with the downregulation of ATP production to reduce HSP70 expression, which can improve PPAB-mediated PTT ablation. Besides, systematic *in vitro* and *in vivo* studies confirm that the PR NPs exhibit excellent stability, superb photothermal performance, desired biosafety, and potent antitumor effect guided by NIR photothermal/fluorescence imaging (PTI/FLI) capability with precise tumor-targeting property, providing a novel perspective for high-efficacy and low-toxicity CRC treatment.

4 Experimental

4.1 Synthetic routes

4.1.1 *Synthesis of DPP-1*

Firstly, the potassium tert-butoxide (1.36 g, 12.08 mmol) with tert-butanol (7 mL) was heated to 108 °C under N_2 protection. The mixture of 2-cyanothiophene (1.00 g, 9.16 mmol), tert-amyl alcohol (3 mL), and dimethyl succinate (0.50 g, 3.40 mmol) was added dropwise and stirred for 1 h until methanol was removed under reduced pressure. After 2 h, the reaction was terminated by methanol (1 mL)/acetic acid (1 mL) at 65 °C. Finally, the reddish-brown DPP-1 was obtained by filtration after overnight settlement at room temperature (RT).

4.1.2 *Synthesis of DAB*

2-Amino-3-hydroxypyridine (1.00 g, 9.08 mmol) and sodium hydride (0.52 g, 21.80 mmol) were dissolved in ultra-dry DMF (68 mL) and stirred under N_2 atmosphere for 2 h. Thereafter, 7-(bromomethyl)-pentadecane (4.16 g, 13.62 mmol) in ultra-dry DMF (4 mL) was slowly added and stirred in the dark for 24 h. Then the solvent was removed, and the crude product was purified by chromatography on silica gel (EA/DCM, V/V = 1:3) to afford the brown oily DAB (1.98 g, 54% yield). ^{1}H NMR (500 MHz, $CDCl_3$): δ 7.60 (d, J = 8.00 Hz, 1H), 6.89 (d, J = 11.50 Hz, 1H), 6.59 (dd, J_1 = 9.50 Hz, J_2 = 6.50 Hz, 1H), 4.89 (s, 2H), 3.85 (d, J = 7.00 Hz, 2H), 1.85–1.74 (m, 1H), 1.32–1.24 (m, 24H), 0.90–0.85 (m, 6H).

4.1.3 *Synthesis of PPAB*

DPP-1 (300.00 mg, 1.00 mmol) and PPAB-1 (1.51 g, 4.50 mmol) were dissolved in anhydrous toluene (60 mL), and stirred at 110 °C for 1 h under N_2 protection. Subsequently, $TiCl_4$ (0.804 mL) was added for 10 min reaction, and triethylamine (2.04 mL) was introduced for another 2 h reaction. Then, boron trifluoride diethyl etherate (1.92 mL) was added to the mixture for a further 18 h reaction at 123 °C. Then the solvent was removed, and the crude product was purified by chromatography on silica gel (PE/DCM, V/V = 1:1) to acquire green PPAB (259.70 mg, 25% yield). ^{1}H NMR (500 MHz, $CDCl_3$): 9.49 (s, 2H), 7.96 (s, 2H), 7.77 (s, 2H), 7.62 (s, 2H), 7.28 (d, J = 3.00 Hz, 2H), 7.80–7.05 (m, 2H), 4.07 (t, J = 8.50 Hz, 4H), 2.19–1.87 (s, 2H), 1.29–1.27 (m, 48H), 0.95–0.80 (m, 12H). MALDI-TOF-MS: calculated for 1028.57, found: 1029.57.

4.2 Preparation of PPAB NPs, RES NPs and PR NPs

PPAB NPs, RES NPs, and PR NPs were prepared by dissolving PPAB (1.00 mg) and/or RES (1.00 mg) in tetrahydrofuran (THF) (1 mL), followed by nanoprecipitation into ddH_2O (8 mL) containing DSPE-$mPEG_{2000}$ (3.00 mg) over 30 min. The mixture was stirred overnight with constant N_2 blasting to remove THF, and the resulting nanoparticle dispersions (green for PPAB and PR NPs, clear and transparent for RES NPs) were obtained via microporous membrane filtration.

4.3 Photothermal effect and photothermal conversion efficiency

To study the photothermal performance of nanomedicine, PR NPs (1 mL) aqueous dispersion was irradiated with different 730 nm laser power densities (0.2, 0.4, 0.6, 0.8, and 1.0 W/cm^2) and different agent concentrations (0, 5, 10, 15, 30, and 60 μM) over 10 min. Subsequently, the photothermal stability of PR NPs (60 μM) was tested by a 730 nm laser (1.0 W/cm^2) in 5 on/off cycles. Additionally, the photothermal conversion efficiency (η) of PR NPs was calculated with ddH_2O as the contrast.

The photothermal conversion efficiency (PCE) was calculated according to the following Eq. (1):

$$\eta = \frac{hS(T_{max} - T_{surr}) - Q_0}{I(1-10^{-A730})} \quad (1)$$

where h is the heat transfer coefficient, S is the surface area of the

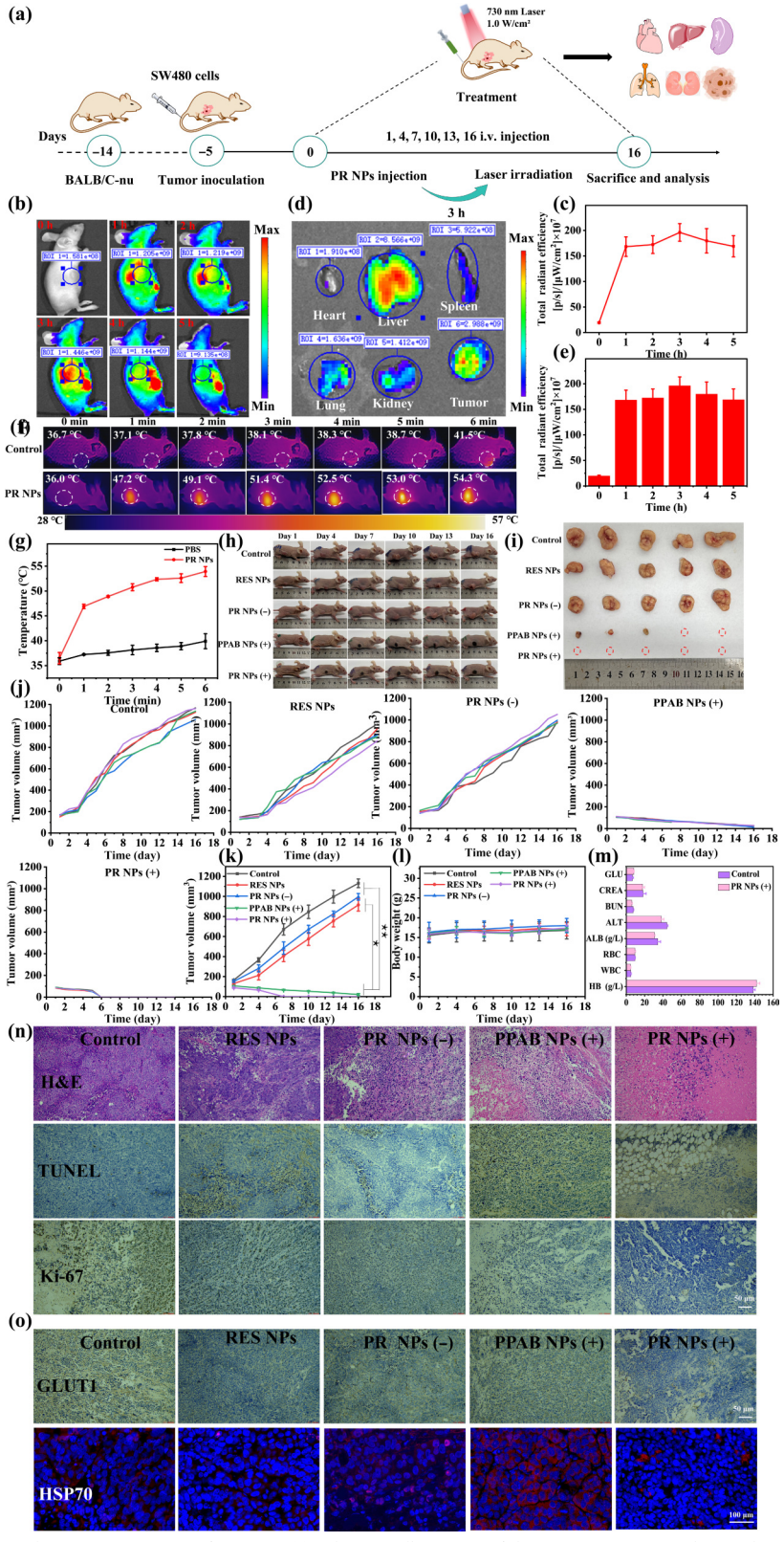

Figure 8 *In vivo* biodistribution and anti-tumor activity of PR NPs. (a) Schematic illustration of the *in vivo* experimental procedure (n = 5). (b) *In vivo* FLI and (c) quantitative analysis of PR NPs at various time points. (d) FLI and (e) quantitative analysis of major organs and tumors at 5 h post-administration of PR NPs. (f) *In vivo* PTI and (g) quantifications analysis of SW480 tumor-bearing mice at 3 h post-administration of PR NPs (+) and PBS (+). (h) and (i) Images of tumor changes during treatment. (j) and (k) Tumor volume changes of all groups after different treatments, n = 5, $^{*}P < 0.05$, $^{**}P < 0.01$. (l) Body weight changes of each nude mouse after different treatments. (m) Hematology, liver, and kidney function tests obtained from different groups. (n) H&E, TUNEL, and Ki-67 staining of tumor tissues following various treatments (scale bar: 50 μm). (o) Immunohistochemical and immunofluorescence staining images of GLUT1 (scale bar: 50 μm) and HSP70 (scale bar: 100 μm) in tumor tissues after different treatments. Data are shown as mean ± SD.

container, and the value of hS is determined from Eq. (2). T_{max} is the steady-state maximum temperature. T_{surr} is the ambient RT. I is the laser power, and A is the absorbance at 730 nm. Q_0 is the energy input by the same solvent without NPs in the same quartz cuvette after laser irradiation.

$$hS = \frac{C_d m_d}{\tau_s} \quad (2)$$

where τ_s represents the characteristic thermal time constant, which can be determined from Eq. (3), and the heat capacity C_d of deionized water is about 4.2 J/(g·K). m_d represents the mass of the dispersion.

$$t = -\tau s \ln(\theta) \quad (3)$$

where t is the cooling time (s). θ is a dimensionless parameter, known as the driving force temperature, calculated using Eq. (4).

$$\theta = \frac{T - T_{surr}}{T_{max} - T_{surr}} \quad (4)$$

4.4 Cell culture and incubation conditions

SW480, GES-1 cells were cultured in 10% RPMI 1640 complete medium, and HCT116, HUVEC, 293T, L929 cells were maintained in 10% DMEM complete medium. All cells were incubated in a constant-temperature incubator at 37 °C and 5% CO_2.

4.5 Toxicity assay *in vitro*

The cytotoxicity of nanodrugs against SW480 cells and normal cells (HUVEC, 293T, L929, GES-1) was detected by MTT assay. All cells were seeded in 96-well plates (8×10^3 cells/well), wherein SW480 cells were divided into laser and dark groups, while HUVEC, 293T, L929, and GES-1 cells were only assigned to the dark group. When the cells reached 80%, different concentrations of nanodrugs (0, 0.5, 1, 2, 3, 4, 5, 6, 7, and 8 μM) were added and followed by 4 h incubation in the dark. Subsequently, the laser group was exposed to laser irradiation (730 nm, 1.0 W/cm²) and continuously cultured for another 12 h before being treated with MTT and dimethyl sulfoxide (DMSO). Then the optical density of each well at 570 nm was measured. Cell viability was calculated according to the equation (Eq. (5), OD: optical density):

$$\text{Cell viability (\%)} = \frac{\text{OD (Experimental group)}}{\text{OD (Control group)}} \times 100\% \quad (5)$$

4.6 Cellular uptake

SW480 cells were seeded in a confocal dish (1×10^5 cells/well), and when the cells reached 80%, PR NPs (8 μM) were added for 4 h incubation in the dark. Subsequently, the cells were fixed and stained for imaging by CLSM. In addition, flow cytometry was employed to detect the intracellular fluorescence of PR NPs at different incubation time points (0, 1, 2, 4, and 8 h).

4.7 Live/dead cell staining

To track live and dead cells by Calcein-AM/PI staining, SW480 cells cultured with PR NPs in four groups (0, 2, 4, and 8 μM) were illuminated with a 730 nm laser (1.0 W/cm²). After 12 h co-incubation, the cells were stained with Calcein-AM/PI solution, and finally photographed using an inverted fluorescence microscope (Calcein-AM excited at 490 nm, PI excited at 525 nm).

4.8 Flow cytometry apoptosis assay

SW480 cells were co-incubated with PR NPs (0, 2, 4, and 8 μM) for 4 h and illuminated by 730 nm (1.0 W/cm²) laser. After 12 h, the cells were stained with Annexin V-FITC/PI and analyzed by flow cytometry to determine the apoptotic rate (Annexin V-FITC/PI excited at 488 nm, PI excited at 525 nm).

4.9 Wound-healing experiment

SW480 cells were seeded in 12-well plates (1×10^5 cells/well), and scratches were created to treat with different concentrations of PR NPs (0, 2, 4, and 8 μM) when cells reached 80%. Then the cells were stained with Calcein-AM at 0, 12, 24, 36, and 48 h post-scratching, respectively. Finally, the scratch healing process was captured with the cell migration rate calculated accordingly (Calcein-AM excited at 490 nm).

4.10 Transwell migration experiment

PR NPs (0, 2, 4, and 8 μM) were co-incubated with SW480 cells in the dark for 4 h until 730 nm laser (1.0 W/cm²) irradiation. After 12 h, the cells were adjusted with a density of 1×10^6 cells/well and reseeded into the upper chamber of Transwell inserts, while the complete medium containing 10% serum was added to the lower chamber for further incubation for 48 h. Subsequently, the cells were fixed, stained, and finally photographed by an inverted fluorescence microscope.

4.11 Mitochondrial morphology observation

To evaluate mitochondrial damage, TEM was employed to observe changes in mitochondrial morphology of cells after different treatments. SW480 cells (5×10^5 cells/well) were seeded in a 6-well plate and divided into control and PR NPs (+) groups. Subsequently, the P treatment group (8 μM) was irradiated with a 730 nm laser (1.0 W/cm²). Finally, the cells were fixed for TEM imaging.

4.12 Detection of mitochondrial membrane potential

The pretreated SW480 cells were incubated with JC-1 using a mitochondrial membrane potential detection kit and photographed via an inverted fluorescence microscope (JC-1 monomer excited at 514 nm, JC-1 aggregates excited at 585 nm).

4.13 Glucose detection experiments

The PR NPs (0, 2, 4, 8 μM) pretreated SW480 cells were irradiated by a 730 nm laser (1.0 W/cm²). After 12 h, the cells were harvested and homogenized to measure absorbance at 505 nm by a glucose assay kit. The calculation of intracellular glucose content according to the equation (Eq. (6)):

$$\text{Glu (mmol/L)} = \frac{A(\text{assay})}{A(\text{standard})} \times 5 \quad (6)$$

where A(assay) is the absorbance of each experimental group, and A(standard) is the absorbance of the glucose standard.

4.14 ATP detection experiment

The PR NPs (0, 2, 4, and 8 μM) pretreated SW480 cells were irradiated by a 730 nm laser (1.0 W/cm²). After 12 h, the ATP content was determined by an ATP assay kit.

4.15 Metabolomics analysis

SW480 cells were inoculated in 6-well plates (5×10^5 cells/well) and divided into a control and 8 μM PR NPs (+) groups. Herein, the treatment group was irradiated with a 730 nm laser (1.0 W/cm^2). Finally, the cells were collected for metabolomic analysis.

4.16 Western blot analysis

The PR NPs (0, 2, 4, and 8 μM) pretreated SW480 cells were irradiated by a 730 nm laser (1.0 W/cm^2). After 12 h, the cells were collected and lysed to prepare protein samples, which were separated by sodium dodecyl sulfate–polyacrylamide gel electrophoresis (SDS-PAGE) gel electrophoresis and transferred onto polyvinylidene difluoride (PVDF) membranes. After blocking at rt for 2 h, the proteins were incubated with the corresponding antibodies to perform chemiluminescence imaging for protein detection.

4.17 Tumor model

The animal study protocol was approved by the Institutional Animal Care and Use Committee of Anhui Medical University. All female nude mice (5 weeks old, 10–18 g) were purchased from the Comparative Medicine Center of Yangzhou University. Afterwards, 100 μL (6×10^6) SW480 cells were subcutaneously seeded into the back of nude mice to construct the tumor model of SW480 nude mice. When the tumors grew to day 7 with a volume reaching 50–100 mm^3, the animal experiment was initiated.

4.18 Fluorescence imaging and IR thermal imaging *in vivo*

Three SW480 nude mice were randomly selected, and 200 μL (120 μM) of PR NPs were injected via the tail vein. The drug fluorescence *in vivo* was captured at 0, 1, 2, 3, 4, and 5 h. After 5 h, the nude mice were sacrificed and dissected to detect the drug fluorescence in major organs and tumor tissues. In addition, SW480 nude mice were randomly divided into the control (200 μL, PBS) and PR NPs (+) (200 μL, 120 μM) groups. After 3 h, the tumor sites were irradiated by a 730 nm laser (1.0 W/cm^2), and the temperature changes were recorded continuously.

4.19 Anti-tumor therapy *in vivo*

SW480 tumor-bearing nude mice were randomly divided into five groups (n = 5/group): (I) Control; (II) RES NPs; (III) PR NPs (–); (IV) PPAB NPs (+); (V) PR NPs (+). When the tumor volume reached 50–100 mm^3, 200 μL of PBS or nanodrug was injected *via* the tail vein, and the laser group was illuminated with a 730 nm laser (1.0 W/cm^2) for 6 min within 3 h post-injection. During the treatment period, tumor volume (length × width^2/2) and body weight were measured every 3 days. Eventually, all mice were sacrificed at 16 days.

4.20 Histochemistry and immunofluorescence analysis

After sacrificing the mice on day 16, major organs (heart, liver, spleen, lung, and kidney) and tumor tissues were harvested for H&E, TUNEL, Ki-67, GLUT1, and HSP70 immunostaining, respectively, which were captured under an optical microscope.

4.21 Routine blood and biochemical tests

The whole blood of tumor-bearing nude mice in the control and PR NPs (+) groups was obtained by orbital blood collection. Then, white blood cell count (WBC), hemoglobin (HGB), and red blood cell count (RBC) were detected, along with relevant liver and kidney function indicators, including alanine aminotransferase (ALT), albumin (ALB), creatinine, glucose, and blood urea nitrogen (BUN).

4.22 Hemolysis experiment

Hemolysis assay was performed to evaluate the biocompatibility of PR NPs. The blood cells (20 μL) were obtained from healthy mice to mix with 1 mL PR NPs (0, 5, 10, 15, 30, 60, and 120 μM), 1 mL ddH_2O (positive control), and 1 mL PBS (negative control), respectively, for 4 h incubation at 37 °C. After the sample photograph, 20 μL of supernatant from each group was collected to measure the absorbance at 542 nm, and the hemolysis rate was calculated according to the following equation (Eq. (7)):

$$\text{Hemolysis rate}\ (\%) = \frac{\text{OD (NPs group)} - \text{OD (negative control)}}{\text{OD (positive control)} - \text{OD (negative control)}} \times 100\% \quad (7)$$

4.23 Statistical analysis

Statistical analysis was performed using origin and GraphPad Prism software. Data are presented as mean ± SD obtained from at least three independent assays unless otherwise noted. Data in different groups were analyzed by two-tailed Student's t-test or one-way ANOVA. The scale bar and sample number (n) are shown in the legend.

Electronic Supplementary Material: Supplementary material (details of experimental materials and compound characterization data (^{1}H NMR, MS spectra), as well as Western blot (WB) and tissue section results) is available in the online version of this article at https://doi.org/10.26599/NR.2026.94908722.

Data availability

All data needed to support the conclusions in the paper are presented in the manuscript and/or the Electronic Supplementary Material. Additional data related to this paper may be requested from the corresponding author upon request.

Acknowledgements

The authors acknowledge the National Natural Science Foundation of China (No. 82102851), Doctoral Start-up Foundation of Anhui Medical University (No. 0801029201), Research Fund of Anhui Institute of Translational Medicine (No. 2023zhyx-C12), and Postgraduate Innovation Research and Practice Program of Anhui Medical University (No. YJS20230146). The authors thank the Center for Scientific Research of School of Life Sciences, Anhui Medical University.

Declaration of competing interest

All the contributing authors report no conflict of interests in this work.

Author contribution statement

Y. L. Z.: Writing – original draft, data curation. Y. J. S.: Writing – review. S. W.: Writing – review. Q. H.: Data curation. M. Z.: Data curation. G. G. Z.: Investigation. M. M. G.: Investigation. K. C. Z.:

Conceptualization, review & editing. D. X. Z.: Conceptualization, review & editing. X. W. W.: Conceptualization, review & editing. P. P. L.: Supervision, writing – original draft, review & editing, funding acquisition. All the authors have approved the final manuscript.

Informed consent

Not applicable.

Ethics statement

All animal experiments were performed in accordance with the regulations on animal experimentation and approved by the ethics committee of Anhui Medical University (Date: 1st March 2021; Approval number: 20210901).

Use of AI statement

None.

References

[1] Bray, F.; Laversanne, M.; Sung, H.; Ferlay, J.; Siegel, R. L.; Soerjomataram, I.; Jemal, A. Global cancer statistics 2022: GLOBOCAN estimates of incidence and mortality worldwide for 36 cancers in 185 countries. *CA Cancer J. Clin.* **2024**, *74*, 229–263.

[2] Lu, D. M.; Dong, C. X.; Wang, K. L.; Ye, C. Y.; Chen, L. B.; Yuan, Y.; Hu, H. G. Updates of CSCO guidelines for colorectal cancer version 2025. *Chin. J. Cancer Res.* **2025**, *37*, 297–302.

[3] Biller, L. H.; Schrag, D. Diagnosis and treatment of metastatic colorectal cancer: A review. *JAMA* **2021**, *325*, 669–685.

[4] Ciardiello, F.; Ciardiello, D.; Martini, G.; Napolitano, S.; Tabernero, J.; Cervantes, A. Clinical management of metastatic colorectal cancer in the era of precision medicine. *CA Cancer J. Clin.* **2022**, *72*, 372–401.

[5] Wu, L. Y.; Rao, W.; Guo, L.; Zhang, F. S.; Li, W. H.; Ying, J. M. Pan-cancer analysis to character the clinicopathological and genomic features of KRAS-mutated patients in China. *J. Cancer Res. Clin. Oncol.* **2025**, *151*, 94.

[6] Zhou, Z. T.; Guo, F. R.; Zhang, J. Y.; Liao, L. F.; Jiang, M. C.; Huang, Y.; Liu, Y.; Lei, L. T. Y.; Tao, Z. H.; Yu, C. Y. et al. Facile integration of a binary nano-prodrug with αPD-L1 as a translatable technology for potent immunotherapy of TNBC. *Acta Biomater.* **2025**, *194*, 373–384.

[7] Chen, Q.; Li, Y. N.; Hu, J. M.; Xu, Z. Y.; Wang, S. Y.; Cai, N. C.; He, M. J.; Xiao, Y. F.; Ding, Y.; Sun, M. J. et al. Local exosome inhibition potentiates mild photothermal immunotherapy against breast cancer. *Adv. Sci.* **2025**, *12*, 2406328.

[8] Dai, H. M.; Pan, J. Y.; Shao, J. J.; Xu, K.; Ruan, X. H.; Mei, A. Q.; Chen, P.; Qu, L. L.; Dong, X. C. Boosting nonradiative decay of boron difluoride formazanate dendrimers for NIR-II photothermal theranostics. *Angew. Chem., Int. Ed.* **2025**, *64*, e202503718.

[9] Guo, Y. H.; Wang, J. Y.; Wu, X. M.; Qiao, Q. Q.; Liao, T.; Li, L. W.; Xu, Z. Q.; Zheng, D. W.; Kuang, Y.; Yu, W. Q. et al. Gold nanoparticle-loaded multifunctional $Ti_3C_2T_x$ MXene nanosheets fabricated by *in situ* reduction to effectively enhance their catalase-like activity for tumor therapy. *Nano Today* **2025**, *65*, 102848.

[10] Zhao, R. R.; Zheng, G. R.; Fan, L. L.; Shen, Z. C.; Jiang, K.; Guo, Y.; Shao, J. W. Carrier-free nanodrug by co-assembly of chemotherapeutic agent and photosensitizer for cancer imaging and chemo-photo combination therapy. *Acta Biomater.* **2018**, *70*, 197–210.

[11] Zheng, W. J.; Bai, L.; Du, N. W.; Zhang, N. N.; Zhu, S. J.; Xu, J. T.; Chen, F.; Tao, H. X.; Li, Z. Z.; Li, M. et al. NIR-II-activated photothermal therapy using gold nanotetrapods enhances antigen presentation and immune response in colorectal cancer. *Nano Res.* **2025**, *18*, 94907970.

[12] Jeon, N.; Kim, L.; Choi, S. G.; Lee, H.; Min, J. Y.; Kim, H. M.; Han, E. H.; Lee, E. Self-assembled peptide-gold nanoparticle 1D nanohybrids functionalized with GHK tripeptide for enhanced wound-healing and photothermal therapy. *ACS Appl. Mater. Interfaces* **2025**, *17*, 15080–15096.

[13] Li, Y. J.; Zhang, Y.; Dong, Y.; Akakuru, O. U.; Yao, X. H.; Yi, J. M.; Li, X. Y.; Wang, L. L.; Lou, X. H.; Zhu, B. Y. et al. Ablation of gap junction protein improves the efficiency of nanozyme-mediated catalytic/starvation/mild‐temperature photothermal therapy. *Adv. Mater.* **2023**, *35*, 2210464.

[14] Zhang, J. Y.; Gai, T. Y.; Wang, J. W.; Wu, Y. C.; Zeng, S. M.; Zhao, D. Y.; Li, W. Nucleic acid‐locked smart carrier for photothermal/chemotherapy‐amplified immunogenic cell death to enhance systemic antitumor efficacy. *Adv. Sci.* **2025**, *12*, 2503299.

[15] Dash, B. S.; Lu, Y. J.; Chen, J. P. Enhancing photothermal/photodynamic therapy for glioblastoma by tumor hypoxia alleviation and heat shock protein inhibition using IR820-conjugated reduced graphene oxide quantum dots. *ACS Appl. Mater. Interfaces* **2024**, *16*, 13543–13562.

[16] Shang, K.; Tang, D. S.; Cui, M. H.; Hou, H.Y.; Xiao, B.; Liu, J. J.; Zhang, R. S.; Kuai, R.; Liu, J. F.; Xiao, H. H. et al. Synthetic high-density lipoprotein mimicking nanodiscs with Pt(IV) prodrug enable tumor targeting and cGAS-STING pathway activation for chemo-immunotherapy. *Adv. Mater.* **2025**, *37*, e06011.

[17] Wang, Y.; Wang, J. L.; Ye, R. M.; Jin, Q. Y.; Yin, F. Y.; Liu, N.; Wang, Y. B.; Zhang, Q.; Gao, T.; Zhao, Y. L. Cancer cell-mimicking Prussian blue nanoplatform for synergistic mild photothermal/chemotherapy via heat shock protein inhibition. *ACS Appl. Mater. Interfaces* **2024**, *16*, 20908–20919.

[18] Xu, K.; Luo, M. C.; Wang, W. L.; Zhang, T.; Chen, Y.; Shao, J. J.; Chen, P.; Dong, X. C.; Cai, Y. Boron difluoride formazanate dye with donor planarization engineering for 1060 nm laser activated photothermal theranostics. *Adv. Sci.* **2025**, *12*, e06226.

[19] Peng, D. Z.; Zhang, Z. B.; Zhang, Q. Y.; Liu, Y. C.; Wang, N. Organic molecule-based nanoparticles for multimodal colorectal cancer therapy: Oxidative stress-induced apoptosis and ferroptosis. *Chem. Eng. J.* **2025**, *511*, 162259.

[20] Jiang, Q. Y.; He, J. H.; Zhang, H. R.; Chi, H. R.; Shi, Y.; Xu, X. L. Recent advances in the development of tumor microenvironment-activatable nanomotors for deep tumor penetration. *Mater. Today Bio* **2024**, *27*, 101119.

[21] Cai, J.; Xu, X.D.; Saw, P. E. Nanomedicine targeting ferroptosis to overcome anticancer therapeutic resistance. *Sci. China Life Sci.* **2024**, *67*, 19–40.

[22] Li, C. L.; Zhang, J. H.; Song, Q.; Wang, Y. T.; Liu, Y. P.; Wang, J. X.; Sun, Y. Next-generation supramolecular photosensitizers based on coordination-driven self-assembly for therapeutic applications. *Acta Biomater.* **2026**, *210*, 549–569.

[23] Ma, P. K.; Wei, G. J.; Chen, J. H.; Jing, Z. Q.; Wang, X.; Wang, Z. J. GLUT1 targeting and hypoxia-activating polymer-drug conjugate-based micelle for tumor chemo-thermal therapy. *Drug Deliv.* **2021**, *28*, 2256–2267.

[24] Wu, X. W.; Fan, Y.; Wang, K. R.; Miao, Y. Q.; Chang, Y. L.; Ming, J.; Wang, X. Y.; Lu, S. W.; Liu, R. C.; Zhang, F. et al. NIR-II imaging-guided precise photodynamic therapy for augmenting tumor-starvation therapy by glucose metabolism reprogramming interference. *Sci. Bull.* **2024**, *69*, 1263–1274.

[25] Zhang, D. Y.; Liang, Y. Q.; Wang, M. C.; Younis, M. R.; Yi, H. X.; Zhao, X. Y.; Chang, J. S.; Zheng, Y.; Guo, W. S.; Yu, X. Y. Self‐assembled carrier-free nanodrugs for starvation therapy‐amplified photodynamic therapy of cancer. *Adv. Healthcare Mater.* **2023**, *12*,

2203177.

[26] Chen, Y. K.; Chen, Y. Y.; Wang, Z. Z.; Yang, L.; Zhang, Y.; Zhang, Z. X.; Jia, L. J. Iron-based MOF with Catalase-like activity improves the synergistic therapeutic effect of PDT/ferroptosis/starvation therapy by reversing the tumor hypoxic microenvironment. *J. Nanobiotechnol.* **2024**, *22*, 705.

[27] Yu, K. X.; Zhou, H.; Xu, Y. M.; Cao, Y. D.; Zheng, Y. Y.; Liang, B. Engineering a triple-functional magnetic gel driving mutually-synergistic mild hyperthermia-starvation therapy for osteosarcoma treatment and augmented bone regeneration. *J. Nanobiotechnol.* **2023**, *21*, 201.

[28] Li, Y. P.; Hong, W. Y.; Zhang, H. N.; Zhang, T. T.; Chen, Z. Y.; Yuan, S. L.; Peng, P.; Xiao, M.; Xu, L. Photothermally triggered cytosolic drug delivery of glucose functionalized polydopamine nanoparticles in response to tumor microenvironment for the GLUT1-targeting chemo-phototherapy. *J. Controlled Release* **2020**, *317*, 232–245.

[29] Lu, S. J.; Tian, H. L.; Li, L.; Li, B. W.; Yang, M.; Zhou, L.; Jiang, H.; Li, Q.; Wang, W. H.; Nice, E. C. et al. Nanoengineering a zeolitic imidazolate framework‐8 capable of manipulating energy metabolism against cancer chemo-phototherapy resistance. *Small* **2022**, *18*, 2204926.

[30] Ma, Y. J.; Wang, F. Q.; Wang, D. W.; He, X. W.; Li, W. Y.; Zhang, Y. K. Near-infrared-triggered release of self-accelerating cascade nanoreactor delivered by macrophages for synergistic tumor photothermal therapy/starvation therapy/chemodynamic therapy. *J. Colloid Interface Sci.* **2025**, *685*, 661–673.

[31] Koo, S.; Lee, M. G.; Sharma, A.; Li, M. L.; Zhang, X. C.; Pu, K. Y.; Chi, S. G.; Kim, J. S. Harnessing GLUT1‐targeted pro‐oxidant ascorbate for synergistic phototherapeutics. *Angew. Chem., Int. Ed.* **2022**, *61*, e202110832.

[32] Li, X. L.; Jiang, C.; Wang, Q. H.; Yang, S. B.; Cao, Y. Y.; Hao, J. N.; Niu, D. C.; Chen, Y.; Han, B.; Jia, X. et al. A "valve-closing" starvation strategy for amplification of tumor-specific chemotherapy. *Adv. Sci.* **2022**, *9*, 2104671.

[33] Li, Z. Y.; Li, X. H.; Ai, S. C.; Liu, S.; Guan, W. X. Glucose metabolism intervention-facilitated nanomedicine therapy. *Int. J. Nanomedicine* **2022**, *17*, 2707–2731.

[34] Buhrmann, C.; Shayan, P.; Brockmueller, A.; Shakibaei, M. Resveratrol suppresses cross-talk between colorectal cancer cells and stromal cells in multicellular tumor microenvironment: A bridge between *in vitro* and *in vivo* tumor microenvironment study. *Molecules* **2020**, *25*, 4292.

[35] Mu, Q.; Najafi, M. Resveratrol for targeting the tumor microenvironment and its interactions with cancer cells. *Int. Immunopharmacol.* **2021**, *98*, 107895.

[36] Ko, J. H.; Sethi, G.; Um, J. Y.; Shanmugam, M. K.; Arfuso, F.; Kumar, A. P.; Bishayee, A.; Ahn, K. S. The role of resveratrol in cancer therapy. *Int. J. Mol. Sci.* **2017**, *18*, 2589.

[37] Yang, S. Y.; Xu, W. Q.; Feng, L. K.; Zhang, C. Y.; Yan, C. Z.; Zhang, J. J.; Lai, J. S.; Yan, T. M.; He, Z.; Du, X. G. et al. Resveratrol improves the digestive ability and the intestinal health of Siberian sturgeon. *Int. J. Mol. Sci.* **2022**, *23*, 11977.

[38] Duan, X. R.; Tian, H. L.; Zheng, S. W.; Zhu, J. M.; Li, C.; He, B.; Li, L.; Jiang, H.; Lu, S. J.; Feng, Y. M. et al. Photothermal‐starvation therapy nanomodulator capable of inhibiting colorectal cancer recurrence and metastasis by energy metabolism reduction. *Adv. Healthcare Mater.* **2023**, *12*, 2300968.

[39] Moutabian, H.; Majdaeen, M.; Ghahramani-Asl, R.; Yadollahi, M.; Gharepapagh, E.; Ataei, G.; Falahatpour, Z.; Bagheri, H.; Farhood, B. A systematic review of the therapeutic effects of resveratrol in combination with 5-fluorouracil during colorectal cancer treatment: With a special focus on the oxidant, apoptotic, and anti-inflammatory activities. *Cancer Cell Int.* **2022**, *22*, 142.

[40] Wu, C. L.; Huang, X. Y.; Tang, Y. Y.; Xiao, W. Y.; Sun, L. G.; Shao, J. J.; Dong, X. C. Pyrrolopyrrole aza-BODIPY near-infrared photosensitizer for dual-mode imaging-guided photothermal cancer therapy. *Chem. Commun.* **2019**, *55*, 790–793.

[41] Kage, Y.; Mori, S.; Ide, M.; Saeki, A.; Furuta, H.; Shimizu, S. Blackening of aza-BODIPY analogues by simple dimerization: Panchromatic absorption of a pyrrolopyrrole aza-BODIPY dimer. *Mater. Chem. Front.* **2018**, *2*, 112–120.

[42] Li, J.; Yang, D.; Lyu, W.; Yuan, Y.; Han, X.; Yue, W. Q.; Jiang, J.; Xiao, Y. P.; Fang, Z. J.; Lu, X. M. et al. A bioinspired photosensitizer performs tumor thermoresistance reversion to optimize the atraumatic mild-hyperthermia photothermal therapy for breast cancer. *Adv. Mater.* **2024**, *36*, 2405890.

[43] Birth, D.; Kao, W. C.; Hunte, C. Structural analysis of atovaquone-inhibited cytochrome bc_1 complex reveals the molecular basis of antimalarial drug action. *Nat. Commun.* **2014**, *5*, 4029.

[44] Wang, Y.; Hu, L. F.; Cui, P. F.; Qi, L. Y.; Xing, L.; Jiang, H. L. Pathologically responsive mitochondrial gene therapy in an allotopic expression-independent manner cures Leber's hereditary optic neuropathy. *Adv. Mater.* **2021**, *33*, 2103307.

[45] Xie, Y.; Hou, W.; Song, X.; Yu, Y.; Huang, J.; Sun, X.; Kang, R.; Tang, D. Ferroptosis: Process and function. *Cell Death Differ.* **2016**, *23*, 369–379.

[46] Wei, X. J.; Han, R. L.; Gao, Y.; Song, P. X.; Guo, Z.; Hou, Y. F.; Yu, J. C.; Tang, K. Q. Boosting energy deprivation by synchronous interventions of glycolysis and oxidative phosphorylation for bioenergetic therapy synergetic with chemodynamic/photothermal therapy. *Adv. Sci.* **2024**, *11*, 2401738.